

Torques on curved atmospheric fibres

F. Candelier,¹ K. Gustavsson,² P. Sharma,³ L. Sundberg,² A. Pumir,^{4,3} G. Bagheri,³ and B. Mehlig²

¹*Aix-Marseille Univ., CNRS, IUSTI, Marseille, France*

²*Department of Physics, Gothenburg University, Gothenburg, SE-40530 Sweden*

³*Max Planck Institute for Dynamics and Self-Organization, 37077 Göttingen, Germany*

⁴*Laboratoire de Physique, ENS de Lyon, Université de Lyon 1 and CNRS, 69007 Lyon, France*

(Dated: October 1, 2024)

Small particles are transported over long distances in the atmosphere, with significant environmental impact. The transport of symmetric particles is well understood, but atmospheric particles, such as curved microplastic fibres or ash particles, are generally asymmetric. This makes the description of their transport properties uncertain. Here, we derive a model for how planar curved fibres settle in quiescent air. The model explains that fluid-inertia torques may align such fibres at oblique angles with gravity as seen in recent laboratory experiments, and shows that inertial alignment is a general and thus important factor for the transport of atmospheric particles.

Introduction.— Atmospheric transport is a major dispersal pathway of microplastic particles [1, 2], with negative environmental impact [3, 4], and potentially affecting cloud-formation processes [5, 6]. Therefore it is important to develop reliable models for particle transport in the atmosphere [3, 7]. A challenge is that atmospheric particles, such as curved microplastic fibres [8, 9], tend to be asymmetric. Theoretical models have focused on symmetric shapes [10, 11], which are now considered in the most advanced numerical models for atmospheric transport [12, 13]. However, shape asymmetry may affect the transport of atmospheric fibers. This aspect is at best taken into account by empirical correlations, derived from experimental measurements [14].

Fluid-inertia torques may align fibres as they settle in the atmosphere. Particle-shape symmetry dictates how this happens: axisymmetric fibres with fore-aft symmetry for example align so that their broad side points down, as they settle in a quiescent fluid at moderate particle Reynolds numbers [15–22]. In this case, only one angle matters (the angle between symmetry vector of the fibre and its centre-of-mass velocity). This mechanism is important in the atmospheric sciences, as it is thought to align symmetric ice platelets and columns in weakly turbulent ice clouds [11, 23–27]. Laboratory experiments in viscous cellular flow [28], in a turbulent water-oil mixture [20], for ensembles of fibres in quiescent and turbulent air [29–31], and for spheroids in quiescent air [32] show that the inertial-torque models work quantitatively for axisymmetric particles with fore-aft symmetry. Moreover, breaking of fore-aft symmetry causes small axisymmetric particles to tilt as they settle [33–36].

Curved atmospheric fibres possess neither fore-aft symmetry nor are they axisymmetric. How do shape asymmetries of curved fibres affect inertial torques and thus the angular dynamics? To answer this question, we developed a model for the angular dynamics of curved microplastic fibres. The model predicts how forces and torques depend on the fibre orientation, parametrised by its tilt angle θ and its spin angle ψ , see Fig. 1(a), as

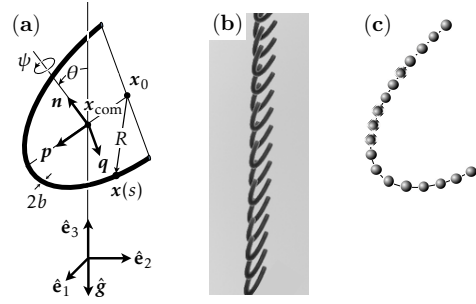


FIG. 1. (a) Particle geometry and definition of particle-fixed coordinate system $\mathbf{p}, \mathbf{q}, \mathbf{n}$. The angles θ and ψ are Euler angles ($Z_\phi Y_\theta Z_\psi$ convention, see supplemental material [37] for details). We refer to θ as the tilt angle, and ψ as the spin angle. For $\phi = \theta = \psi = 0$, the system $\mathbf{p}, \mathbf{q}, \mathbf{n}$ aligns with the lab system $\hat{\mathbf{e}}_1, \dots, \hat{\mathbf{e}}_3$. Also shown is the origin \mathbf{x}_0 of the particle-fixed coordinate system, the centre-of-mass \mathbf{x}_{com} , and the two radii of the fibre, b and R . (b) Stacked video stills of microplastic fibre settling in air with an oblique tilt angle, data from Ref. [14]. Gravity $\hat{\mathbf{g}}$ points down. (c) Illustration of the model used in the Stokes limit, consisting of hydrodynamically interacting beads.

well as its shape and size. The model explains why current transport models for atmospheric fibres [10, 12, 13] work for the component of the settling speed in the direction of gravity, but fail to describe the sensitive shape-dependence of the angular dynamics seen in the experiments [14]. In particular, fibres may align at oblique angles [Fig. 1(b)], resulting for example in fibre transport perpendicular to gravity. More generally, our results highlight how shape asymmetry affects the delicate effects of fluid inertia for typical atmospheric particles.

Model.— Newton’s equations of motion read

$$\frac{d}{dt} \mathbf{x}_{\text{com}} = \mathbf{v}, \quad m \dot{\mathbf{v}} = \mathbf{F}_h + \mathbf{F}_g, \quad (1a)$$

$$\frac{d}{dt} \mathbf{n} = \boldsymbol{\omega} \wedge \mathbf{n}, \quad \frac{d}{dt} \mathbf{p} = \boldsymbol{\omega} \wedge \mathbf{p}, \quad \frac{d}{dt} (\mathbb{J} \boldsymbol{\omega}) = \mathbf{T}_h. \quad (1b)$$

with mass m , centre of mass \mathbf{x}_{com} and inertia tensor \mathbb{J} of the fibre, gravity force $\mathbf{F}_g = m\mathbf{g}$, hydrodynamic force \mathbf{F}_h and torque \mathbf{T}_h . The vectors \mathbf{p}, \mathbf{q} , and \mathbf{n} denote the

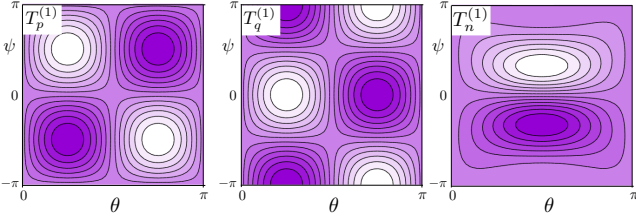


FIG. 2. *Inertial torques for the semi-circular fibre.* Shown are the angular dependencies of $T_p^{(1)}/T_p^{(1,\max)}$, $T_q^{(1)}/T_q^{(1,\max)}$, and $T_n^{(1)}/T_n^{(1,\max)}$ of the inertial torque around the three axes of the particle-fixed coordinate system, obtained from Eq. (3) for $\hat{\mathbf{v}} = -\hat{\mathbf{e}}_3$ ($\hat{v}_p = \sin\theta \cos\psi$, $\hat{v}_q = -\sin\theta \sin\psi$, and $\hat{v}_n = -\cos\theta$). Colourbar: from -1 (white) to 1 (violet).

particle-fixed coordinate system [Fig. 1(a)]. We consider fibres in the form of circle segments with different radii of curvature, R . Examples are semi-circular fibres and quarter circles. The fibre diameter is denoted by $2b$, the contour length by $2a$. The aspect ratio is $\kappa = a/b$.

Stokes limit.— In a quiescent fluid, the Stokes force and torque on the particle are [38]:

$$\begin{bmatrix} \mathbf{F}_h^{(0)} \\ \mathbf{T}_h^{(0)} \end{bmatrix} = -\mu \begin{bmatrix} \mathbb{A} & \mathbb{B}^T \\ \mathbb{B} & \mathbb{C} \end{bmatrix} \begin{bmatrix} \mathbf{v} \\ \boldsymbol{\omega} \end{bmatrix}. \quad (2)$$

Here \mathbf{v} is the centre-of-mass velocity, $\boldsymbol{\omega}$ is the angular velocity around \mathbf{x}_{com} , μ is the dynamic viscosity of the fluid, and $\mathbb{A}, \mathbb{B}, \mathbb{C}$ are resistance tensors. These tensors are constrained by particle-shape symmetries [39, 40]. Two reflection symmetries cause all elements of \mathbb{B} to vanish in the particle-fixed coordinate system, except $B_{qn} = \mathbf{q} \cdot \mathbb{B}\mathbf{n}$, and B_{nq} . The tensors \mathbb{A} and \mathbb{C} are diagonal in this coordinate system.

In order to determine how the fibres settle in the Stokes limit, we seek the steady states of Eqs. (1) with $\mathbf{F}_h = \mathbf{F}_h^{(0)}$ and $\mathbf{T}_h = \mathbf{T}_h^{(0)}$. This is accurate when the particle Reynolds number $\text{Re}_a = av^*/\nu$ is very small, where v^* is the steady-state settling speed of the fibre, and ν is the kinematic viscosity of air. Setting $\dot{\mathbf{v}} = \dot{\mathbf{n}} = \dot{\mathbf{p}} = \dot{\boldsymbol{\omega}} = 0$ in Eqs. (1) yields two steady states: $(\theta^*, \psi^*) = (\pi/2, 0)$ (\mathbf{p} points down), and $(\pi/2, \pi)$ (\mathbf{p} points up). Both steady states have $\boldsymbol{\omega}^* = 0$ and $\mathbf{v}^* = (0, 0, -v_g^*)$ with $v_g^* = mg/(\mu A_{pp})$. Linear stability analysis shows that the stability of the steady states depends on the signs of B_{qn} and B_{nq} (see supplemental material (SM) [37] for details). We computed the non-zero elements of the resistance tensors using the method of Durlofsky [41–43], modelling the fibres as chains of hydrodynamically interacting beads with radius b [Fig. 1(c)]. This gives $B_{qn} > 0$ and $B_{nq} < 0$ (Table S1 in the SM [37]). In this case, $\psi^* = 0$ is stable, while $\psi^* = \pi$ is unstable. So the fibres settle with \mathbf{n} orthogonal to the settling velocity, and \mathbf{p} points down.

Fluid-inertia torque.— At larger Re_a , the Stokes approximation fails because fluid-inertia torques affect the

angular dynamics. We calculated the fluid-inertia torque for our curved fibres by expanding slender-body theory [16] to order $\text{Re}_a = av^*/\nu$. In the (right-handed) particle-fixed coordinate system from Fig. 1(a) we find:

$$T_{p,M}^{(1)}/(2\pi\mu\nu a^2) = \frac{av}{\nu(\log\kappa)^2} a_{p,M} \hat{v}_q \hat{v}_n, \quad (3a)$$

$$T_{q,M}^{(1)}/(2\pi\mu\nu a^2) = \frac{av}{\nu(\log\kappa)^2} a_{q,M} \hat{v}_p \hat{v}_n, \quad (3b)$$

$$T_{n,M}^{(1)}/(2\pi\mu\nu a^2) = \frac{av}{\nu(\log\kappa)^2} [a_{n,M} \hat{v}_q \hat{v}_p + b_{n,M} \hat{v}_q + c_{n,M} \hat{v}_q \hat{v}_n^2 + d_{n,M} \hat{v}_q^3]. \quad (3c)$$

Here $\hat{v}_p = \mathbf{p} \cdot \hat{\mathbf{v}}$ with $\hat{\mathbf{v}} = \mathbf{v}/v$, and so forth. The parameter M parameterises the central angle $2\pi/M$ of the circle segment ($M = 2$ for a semi circle, $M = 4$ for a quarter circle). The radius of curvature is $R = aM/\pi$. The coefficients $a_{p,M}, a_{q,M}, \dots$ are given in the SM [37]. Fig. 2 shows the angular dependence of the fluid-inertia torque (3) for a semi-circular fibre with $\hat{\mathbf{v}} = -\hat{\mathbf{e}}_3$.

Circle segments lack fore-aft symmetry and axisymmetry, but the remaining shape symmetry constrains how the components T_p, T_q, T_n of the torque in the particle-fixed coordinate system depend on the components of the settling velocity \mathbf{v} . Covariance under coordinate change implies that T_p is even in \hat{v}_p , but odd in \hat{v}_q and \hat{v}_n . Corresponding conclusions hold for T_q and T_n . Shape symmetry constrains the possible terms in Eq. (3) further, but allows for terms that do not occur there (the corresponding coefficients vanish). The reason may be that the slender-body approximation for $\mathbf{T}^{(1)}$ neglects hydrodynamic interactions between different parts of the fibre to order $(\log\kappa)^{-2}$ [42, 44].

To understand how fluid inertia changes the angular dynamics, we search for steady states using $\mathbf{F}_h = \mathbf{F}_h^{(0)}$ and $\mathbf{T}_h = \mathbf{T}_h^{(0)} + \mathbf{T}_h^{(1)}$ in Eqs. (1), neglecting Re_a -corrections to the force at first. Symmetry implies that $v_q^* = 0$ and $\psi^* = 0$. Thus we seek solutions of

$$0 = -\mu A_{pp} v_p + mg \sin\theta, \quad (4a)$$

$$0 = -\mu A_{nn} v_n - mg \cos\theta, \quad (4b)$$

$$0 = -\mu B_{qn} v_n + \frac{\mu a^3}{\nu(\log\kappa)^2} 2\pi a_{q,M} v_p v_n. \quad (4c)$$

Eqs. (4) admit two steady states, one with $v_n^* = 0$, and the other one with $v_n^* \neq 0$. The first steady state is stable when $T_q^{(1)}$ is weak enough, and it is the same as in the Stokes limit: $\theta^* = \pi/2$, $\psi_1^* = 0$, $v_q^* = v_n^* = 0$, and $v_p^* = v_g^* = mg/(\mu A_{pp})$. This fixed point becomes unstable in a pitchfork bifurcation as the fluid-inertia torque increases. The bifurcation occurs when

$$A'_{pp} B'_{qn} (\log\kappa)^2 = 2\pi a_{q,M} \mathcal{R} \mathcal{V}. \quad (5)$$

Here we use non-dimensional variables and parameters: $A'_{pp} = A_{pp}/a$, $B'_{qn} = B_{qn}/a^2$, the particle-to-fluid mass-density ratio $\mathcal{R} = \rho_p/\rho_f$, and $\mathcal{V} = 2\pi ab^2 g/\nu^2 = \pi d_{\text{eq}}^3 g/(6\nu^2)$, a non-dimensional volume [32], and d_{eq} is

the volume-equivalent diameter of the fibre. The product $\mathcal{R}\mathcal{V}$ is proportional to Ga^2 . The Galileo number Ga measures the ratio of gravity to viscous forces. For small particle Reynolds numbers, $\mathcal{R}\mathcal{V} \propto \text{Re}_a$ up to a geometry-dependent factor. Thus larger $\mathcal{R}\mathcal{V}$ implies larger fluid-inertia torques. Beyond the bifurcation – for large enough $\mathcal{R}\mathcal{V}$ – two stable steady states form, with stable orientation

$$\theta^* = \arcsin\left(\frac{A'_{pp}B'_{qn}(\log \kappa)^2}{2\pi a_{q,m}\mathcal{R}\mathcal{V}}\right) \quad (6)$$

(and the equivalent $\pi - \theta^*$ due to symmetry). We conclude: the plane containing the curved fibre in its steady state orientation tilts when the argument of arcsin in Eq. (6) is smaller than unity, so that $\theta^* \neq \pi/2$. Eq. (6) for θ^* is qualitatively similar to that for axisymmetric particles with broken fore-aft symmetry [33, 34, 36]. For the curved fibres, Eq. (6) is a consequence of broken symmetry under $\mathbf{p} \rightarrow -\mathbf{p}$. We note that fluid inertia does not change the value of ψ^* .

Experimental data.– Using the Göttingen turret [32], Tatsii *et al.* [14] measured the settling speeds of curved fibres (quarter and semi circles) with different lengths L and aspect ratios κ , and mass density $\rho_p = 1200 \text{ kg/m}^3$, comparable to that of common microplastic fibres in the

TABLE I. Summary of experimental results for semi- and quarter-circular fibres. Parameters: contour length $2a$ [mm], diameter $2b$ [mm], average settling speed $\langle v_g \rangle$ [m/s] from Table 1 in Ref. [14], experimental particle Reynolds number $\text{Re}_a \approx a\langle v_g \rangle/\nu$, with kinematic viscosity of air $\nu = 1.5 \times 10^{-5} \text{ m}^2/\text{s}$, inertia parameter $\mathcal{R}\mathcal{V}$ (see text). Steady-state angles ψ^* [rad] and θ^* [rad] [Fig. 1(a)] extracted from the data [14] as described in the SM [37]. Number N of experiments analysed.

κ	$2a$	$2b$	$\langle v_g \rangle$	Re_a	$\mathcal{R}\mathcal{V}$	ψ^*	θ^*	N
semi-circular fibres								
20	2	0.1	0.704	47	660	– ^a	– ^a	9
	1	0.05	0.288	9.6	83	0.013±0.024	1.21±0.1	8
50	2	0.04	0.218	14.5	110	0	0.79	1
	1	0.02	0.086	2.9	13	0	1.54	1
100	2	0.02	0.094	6.2	26	0	1.48±0.13	5
	1	0.01	0.037	1.24	3.3	* ^b	* ^b	0
quarter-circular fibres								
20	2	0.1	0.631	42	660	– ^a	– ^a	8
	1	0.05	0.265	8.8	83	-0.03±0.01	1.34±0.13	10
	0.5	0.025	0.096	1.6	10	-0.017	1.414	1
50	2	0.04	0.209	14.0	110	-0.003±0.017	1.48±0.06	11
	1	0.02	0.074	2.5	13	0	1.43±0.07	2
100	2	0.02	0.080	5.3	26	0	1.379	1
	1	0.01	0.026	0.88	3.3	* ^b	* ^b	0

^a ‘–’ no steady state observed.

^b ‘*’ fibre images blurred, orientations could not be determined.

atmosphere. Here we extracted the angular dynamics from the video recordings (see SM [37] for details). The results (Table I) are qualitatively consistent with the theory outlined above, except for the fibres with the largest fluid-inertia parameters $\mathcal{R}\mathcal{V}$ which do not align. As predicted by the theory, all other fibres settle with steady orientations with $\psi^* = 0$. For quarter circles, the steady tilt angle is $\theta^* \approx \pi/2$, so $\mathcal{R}\mathcal{V}$ is below the bifurcation analysed above. Semi-circular fibres, by contrast, settle with a $\mathcal{R}\mathcal{V}$ -dependent tilt angle. As predicted by the theory, $\theta^* \approx \pi/2$ for small $\mathcal{R}\mathcal{V}$, and θ^* decreases as $\mathcal{R}\mathcal{V}$ increases.

For a quantitative comparison, the model must be improved to account for the fact that Re_a is not small in the experiment, so that the small- Re_a theory (3) does not directly apply. Moreover, we expect that fluid-inertia corrections to the force – neglected above – may be significant. To improve the model, we computed the fluid-inertia corrections to torque and force in the full slender-body theory [16] by numerical integration of Eqs. (S13), (S14), and (S19) in the SM [37]. Then we searched for steady-state values \mathbf{v}^* and θ^* numerically, for the fibres listed in Table I. The results of these calculations are summarised in Figure 3. Panels (a) and (b) compare the experimental $\langle v_g \rangle$ (Fig. 2a in Ref. [20]) for the fibres from Table I with the full theory for the gravity component v_g^* of the steady settling velocity, as functions of the fluid-inertia parameter $\mathcal{R}\mathcal{V}$. We observe excellent agreement.

Panel (c) compares the theory for θ^* with the experiments for semi-circular fibres. For small $\mathcal{R}\mathcal{V}$, the Stokes torque dominates, yielding stable settling $\theta^* = \pi/2$. For larger $\mathcal{R}\mathcal{V}$, the fibres settle at oblique angles with gravity. Compared with the experiment, theory gives smaller values of θ^* in the transition region between small and large $\mathcal{R}\mathcal{V}$. Here the steady-state tilt angle is sensitive to the precise form of the hydrodynamic torque, as evident from the estimate of the theoretical uncertainty shown in panel (c) (see discussion below). Panel (d) shows that the theory works well for the quarter circles too. For $\mathcal{R}\mathcal{V} = 660$, quarter and semi circles continue to tumble in the experiments. Our model indicates that this may be explained by a second bifurcation around $\mathcal{R}\mathcal{V} = 660$ that results in either a long transient towards, or a change of stability of θ^* .

Discussion.– Our model shows that the component v_g^* of the settling velocity is almost independent of the non-dimensional radius of curvature R/a , and only weakly dependent on its aspect ratio κ , in agreement with the experiment [Fig. 3(a,b) and Table I]. For slender fibres, the weak κ -dependence is explained because the aspect ratio enters only as $\log \kappa$ in the model (at fixed \mathcal{V}). The weak dependence on R/a is explained by the fact that the elements of \mathbb{A} are similar for quarter and semi circles, and that the M -dependence of the fluid-inertia force compensates for this dependence, in part. In summary, our model shows that the variation of v_g^* for different fibres is mainly determined by the parameter $\mathcal{R}\mathcal{V}$. We conclude:

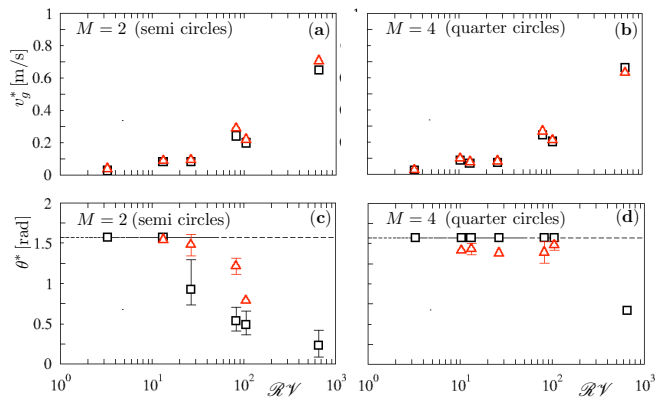


FIG. 3. *Comparison between theory and experiment* (Table I). (a) Full slender-body theory (see text) for v_g^* for semi-circular fibres versus the inertia parameter $\mathcal{R}\mathcal{V}$ (\square); experimental $\langle v_g \rangle$ (red \triangle). (b) same, but for quarter circles. (c) Theory for steady-state tilt angle θ^* for semi-circular fibres (\square). Estimated theoretical uncertainties (see text) are shown when larger than the symbol size. Experiment (red \triangle) with errors from Table I. Dashed line corresponds to $\theta^* = \frac{\pi}{2}$. (d) same, but for quarter circles (theoretical uncertainty not shown).

this is the most important parameter for empirical settling models for slender fibres (but note that g_g^* for a slender fibre differs from that of a sphere of equivalent volume [10, 14, 32]).

Regarding the angular dynamics, the conclusions are quite different. The experiments show that curved fibres settle at a steady tilt angle θ^* that depends sensitively on the non-dimensional radius of curvature R/a , as well as on $\mathcal{R}\mathcal{V}$. In particular, quarter and semi circles settle quite differently [Fig. 3(c),(d)] for the same size and value of $\mathcal{R}\mathcal{V}$. Our theory shows that this difference is a consequence of the bifurcation. The Stokes torque decreases more slowly than the fluid-inertia torque as one straightens the fibre by increasing R/a , shifting the location of the bifurcation for quarter circles to larger values of $\mathcal{R}\mathcal{V}$. Beyond the bifurcation, the model predicts significant motion perpendicular to gravity that is not explained by existing empirical models. We find $v_{\perp}/v_g \approx 0.13$ to 0.15 for the first three data points after the bifurcation in Fig. 3(c). In conclusion, atmospheric transport models for slender fibres must account not only for $\mathcal{R}\mathcal{V}$, but also for the radius of curvature.

The theory also explains why fluid inertia does not change the spin angle, it remains $\psi^* = 0$ as in the Stokes limit. This follows from the shape symmetry of the fibre. But note that imperfections (shape asymmetries or density inhomogeneities) may break this symmetry, causing the steady-state angle ψ^* to change, distorting the patterns in Fig. 2. Note also that non-planar fibres may continue to rotate in the Stokes limit [45], like chiral ribbons [43] and taco-shaped disks [46]. How fluid inertia affects this dynamics is not known.

Overall, Fig. 3 shows good agreement between model and experiment, except near the bifurcation, where the tilt angle is sensitive to the details of the hydrodynamic torque. We stress that the model does not contain any fitting parameters, unlike that in e.g. Ref. [32].

We now discuss possible shortcomings of the full model, and the deviations between model and experiment for θ^* near the bifurcation. For straight cylinders, Fintzi *et al.* [47] assessed the accuracy of slender-body theory by DNS, comparing to Ref. [16], and to higher-order calculations [48]. They find that the theory of Khayat and Cox [16] fails to quantitatively account for contributions to force and torque from the lateral surfaces (end caps) of the cylinder for $\text{Re}_a > 1$ and $\kappa < 30$. The upstream end cap causes larger deviations than the downstream one. Since the end caps of our steadily settling fibres tend to lie downstream, we expect slender-body theory to work somewhat better for that orientation. Near the bifurcation, θ^* depends sensitively on forces and torques, therefore it is hard to say whether these shortcomings of slender-body theory increase or decrease θ^* . For this reason, we include an estimate of the theoretical uncertainty in Fig. 3(c), showing by how much θ^* changes when increasing/decreasing fluid-inertia torque and force by $\pm 10\%$. Slender-body theory for the Stokes torque requires even larger values of κ [44]. We avoided the latter problem by computing the Stokes torque using the method of Ref. [41].

In some cases, the experiments show that steady-state alignment is approached in an oscillatory fashion, for example as $\psi(t) \sim \cos(\omega t + \varphi) \exp(-\lambda t)$ (Fig. S3 in the SM [37]). This is qualitatively explained by linear stability theory in the Stokes limit. Fluid inertia, however, is expected to have a significant effect on the transient. This remains to be worked out.

For the largest values of $\mathcal{R}\mathcal{V}$, the experiments show unsteady angular dynamics (no steady state within ~ 30 s, Fig. S2 in the SM [37]). This is analogous to the DNS results of Auguste *et al.* [49] and the experiments of Tinklenberg *et al.* [50] for disks settling at $\text{Re} \sim 100$, where periodic angular dynamics can coexist with steady alignment. Our model may qualitatively explain such behaviour, because our numerics indicates that there is a second bifurcation near $\mathcal{R}\mathcal{V} = 660$ where oblique settling becomes unstable. However, the DNS results for straight fibres of Fintzi *et al.* [47] indicate that our model is at best qualitatively correct for $\mathcal{R}\mathcal{V} = 660$.

Conclusions.— Microplastic fibres in the atmosphere settle rapidly because their mass density is about 1000 times higher than that of air. Particle Reynolds numbers based on the fibre half-length are of order 10 for 1mm fibres. Since such fibres tend to be curved, we analysed through model calculations how curvature affects the settling dynamics of curved fibres. Our model explains why curved fibres may align at oblique angles, depending intricately on their shapes, causing transport

perpendicular to the settling direction. The model exemplifies how shape-symmetry breaking affects the angular dynamics of atmospheric particles. This is important because such particles are often asymmetric, just like the curved fibres discussed here, atmospheric ice-crystals which usually have imperfections that break shape symmetries [51], and volcanic-ash particles. For atmospheric particles with highly irregular shapes it may be of interest to generalise the present model to random aggregates.

The angular dynamics of symmetric particles settling in turbulent air has recently been studied in detail [11, 32, 52]. Asymmetric particles can exhibit intricate dynamics in the Stokes limit [9, 53]. In turbulent air, we expect that particle and fluid inertia change the dynamics more than in quiescent air, so the effects discussed here must be accounted for in transport models for atmospheric particles. To conclude, we stress that the conceptually simple case of curved fibres considered here is only one example of the many asymmetric shapes found in the atmosphere, and that the present study uncovers essential physics relevant for a broad class of atmospheric particles.

This work was supported by Vetenskapsrådet under grant nos. 2021-4452 (BM,LS), 2018-03974 and 2023-03617 (KG). FC thanks J. Gissinger for testing the implementation of the bead model. We thank E. Bodenschatz for support and discussions.

-
- [1] S. Allen, D. Allen, F. Baladima, V.R. Phoenix, J.L. Thomas, G. Le Roux, and J.E. Sonke, “Evidence of free tropospheric and long-range transport of microplastic at Pic du Midi Observatory,” *Nature communications* **12**, 7242 (2021).
- [2] Y. Zhang, S. Kang, S. Allen, D. Allen, T. Gao, and M. Sillanpää, “Atmospheric microplastics: A review on current status and perspectives,” *Earth-Science Reviews* **203**, 103118 (2020).
- [3] D. Allen, S. Allen, S. Abbasi, A. Baker, M. Bergmann, J. Brahney, T. Butler, R.A. Duce, S. Eckhardt, N. Evangeliou, *et al.*, “Microplastics and nanoplastics in the marine-atmosphere environment,” *Nature Reviews Earth & Environment* **3**, 393–405 (2022).
- [4] J.C. Prata, J.P. da Costa, I. Lopes, A.C. Duarte, and T. Rocha-Santos, “Environmental exposure to microplastics: An overview on possible human health effects,” *Science of the total environment* **702**, 134455 (2020).
- [5] M. Aeschlimann, G. Li, Z.A. Kanji, and D.M. Mitrano, “Potential impacts of atmospheric microplastics and nanoplastics on cloud formation processes,” *Nature Geoscience* **15**, 967–975 (2022).
- [6] L.E. Revell, P. Kuma, E.C. Le Ru, W.R.C. Somerville, and S. Gaw, “Direct radiative effects of airborne microplastics,” *Nature* **598**, 462–467 (2021).
- [7] J. Brahney, N. Mahowald, M. Prank, G. Cornwell, Z. Klimont, H. Matsui, and K. A. Prather, “Constraining the atmospheric limb of the plastic cycle,” *PNAS* **118**, 1–10 (2021).
- [8] Y. Cai, D.M. Mitrano, M. Heuberger, R. Hufenus, and B. Nowack, “The origin of microplastic fiber in polyester textiles: The textile production process matters,” *Journal of Cleaner Production* **267**, 121970 (2020).
- [9] V. Giurgiu, G.C.A. Caridi, M. De Paoli, and A. Soldati, “Full rotational dynamics of plastic microfibers in turbulence,” *Phys. Rev. Lett.* **133**, 054101 (2024).
- [10] S. Xiao, Y. Cui, J. Brahney, N. M. Mahowald, and Q. Li, “Long-distance atmospheric transport of microplastic fibres influenced by their shapes,” *Nature Geoscience* **16**, 863–870 (2023).
- [11] K. Gustavsson, M. Z. Sheikh, A. Naso, A. Pumir, and B. Mehlig, “Effect of particle inertia on the alignment of small ice crystals in turbulent clouds,” *Journal of the Atmospheric Sciences* **78**, 2573 – 2587 (2021).
- [12] F. Beckett, E. Rossi, B. Devenish, C. Witham, and C. Bonadonna, “Modelling the size distribution of aggregated volcanic ash and implications for operational atmospheric dispersion modelling,” *Atmospheric Chemistry and Physics* **22**, 3409–3431 (2022).
- [13] L. Bakels, D. Tatsii, A. Tipka, R. Thompson, M. Dütsch, M. Blaschek, P. Seibert, K. Baier, S. Bucci, Cassiani, *et al.*, “Flexpart version 11: Improved accuracy, efficiency, and flexibility,” *EGUosphere* **2024**, 1–50 (2024).
- [14] D. Tatsii, S. Bucci, T. Bhowmick, J. Guettler, L. Bakels, G. Bagheri, and A. Stohl, “Shape matters: Long-range transport of microplastic fibers in the atmosphere,” *Environmental Science & Technology* **58**, 671–682 (2024).
- [15] R.G. Cox, “The steady motion of a particle of arbitrary shape at small Reynolds numbers,” *Journal of Fluid Mechanics* **23**, 625–643 (1965).
- [16] R.E. Khayat and R.G. Cox, “Inertia effects on the motion of long slender bodies,” *Journal of Fluid Mechanics* **209**, 435–462 (1989).
- [17] G. Subramanian and Donald L. Koch, “Inertial effects on fibre motion in simple shear flow,” *Journal of Fluid Mechanics* **535**, 383–414 (2005).
- [18] V. Dabade, N. K. Marath, and G. Subramanian, “Effects of inertia and viscoelasticity on sedimenting anisotropic particles,” *J. Fluid Mech.* **778**, 133–188 (2015).
- [19] U. Menon, A. Roy, S. Kramel, G. Voth, and D. Koch, “Theoretical predictions of the orientation distribution of high-aspect-ratio, inertial particles settling in isotropic turbulence,” Abstract Q36.00011, 70th Annual Meeting of the APS Division of Fluid Dynamics, Denver, Colorado (2017).
- [20] A. Roy, S. Kramel, U. Menon, G.A. Voth, and D.L. Koch, “Orientation of finite Reynolds number anisotropic particles settling in turbulence,” *Journal of Non-Newtonian Fluid Mechanics* **318**, 105048 (2023).
- [21] F. Cabrera, M. Z. Sheikh, B. Mehlig, N. Plihon, M. Bourgoïn, A. Pumir, and A. Naso, “Experimental validation of fluid inertia models for a cylinder settling in a quiescent flow,” *Phys. Rev. Fluids* **7**, 024301 (2022).
- [22] F. Jiang, L. Zhao, H. I. Andersson, K. Gustavsson, A. Pumir, and B. Mehlig, “Inertial torque on a small spheroid in a stationary uniform flow,” *Phys. Rev. Fluids* **6**, 024302 (2021).
- [23] K. Sassen, “Remote sensing of planar ice crystal fall attitudes,” *Journal of the Meteorological Society of Japan. Ser. II* **58**, 422–429 (1980).
- [24] J. D. Klett, “Orientation model for particles in turbulence,” *Journal of Atmospheric Sciences* **52**, 2276 – 2285 (1995).

- [25] F.-M. Bréon and B. Dubrulle, “Horizontally oriented plates in clouds,” *Journal of the Atmospheric Sciences* **61**, 2888–2898 (2004).
- [26] V. Noel and K. Sassen, “Study of planar ice crystal orientations in ice clouds from scanning polarization lidar observations,” *Journal of Applied Meteorology* **44**, 653–664 (2005).
- [27] K. Gustavsson, M. Z. Sheikh, D. Lopez, A. Naso, A. Pumir, and B. Mehlig, “Effect of fluid inertia on the orientation of a small prolate spheroid settling in turbulence,” *New Journal of Physics* **21**, 083008 (2019).
- [28] D. Lopez and E. Guazzelli, “Inertial effects on fibers settling in a vortical flow,” *Phys. Rev. Fluids* **2**, 024306 (2017).
- [29] R. K. Newsom and C. W. Bruce, “The dynamics of fibrous aerosols in a quiescent atmosphere,” *Physics of Fluids* **6**, 521–530 (1994).
- [30] R.K. Newsom and C.W. Bruce, “Orientational properties of fibrous aerosols in atmospheric turbulence,” *Journal of Aerosol Science* **29**, 773–797 (1998).
- [31] J.-L. Pierson, “Inertial settling of an arbitrarily oriented cylinder in a quiescent flow: From short-time to quasisteady motion,” *Phys. Rev. Fluids* **8**, 104301 (2023).
- [32] T. Bhowmick, J. Seesing, K. Gustavsson, J. Guettler, Y. Wang, A. Pumir, B. Mehlig, and G. Bagheri, “Inertia induces strong orientation fluctuations of nonspherical atmospheric particles,” *Phys. Rev. Lett.* **132**, 034101 (2024).
- [33] F. Candelier and B. Mehlig, “Settling of an asymmetric dumbbell in a quiescent fluid,” *Journal of Fluid Mechanics* **802**, 174–185 (2016).
- [34] A. Roy, R.J. Hamati, L. Tierney, D.L. Koch, and G.A. Voth, “Inertial torques and a symmetry breaking orientational transition in the sedimentation of slender fibres,” *Journal of Fluid Mechanics* **875**, 576–596 (2019).
- [35] S. Ravichandran and J. S. Wettlaufer, “Orientation dynamics of two-dimensional concavo-convex bodies,” *Phys. Rev. Fluids* **8**, L062301.
- [36] Z. Maches, M. Houssais, A. Sauret, and E. Meiburg, “Settling of two rigidly connected spheres,” (2024), arXiv:2406.10381.
- [37] See Supplemental Material at [URL from publisher] for detailed information regarding the theory, the analysis of the video recordings, and the results of this analysis. It contains Ref. [54].
- [38] S. Kim and S.J. Karrila, *Microhydrodynamics: principles and selected applications* (Butterworth-Heinemann, Boston, 1991).
- [39] J. Happel and H. Brenner, *Low Reynolds Number Hydrodynamics* (Martinus Nijhoff Publishers, Hague, 1983).
- [40] J. Fries, J. Einarsson, and B. Mehlig, “Angular dynamics of small crystals in viscous flow,” *Phys. Fluids* **2**, 014302 (2017).
- [41] L. Durlofsky, J. F. Brady, and G. Bossis, “Dynamic simulation of hydrodynamically interacting particles,” *Journal of Fluid Mechanics* **180**, 21–9 (1987).
- [42] D. Collins, R.J. Hamati, F. Candelier, K. Gustavsson, B. Mehlig, and G.A. Voth, “Lord Kelvin’s isotropic helicoid,” *Physical Review Fluids* **6**, 074302 (2021).
- [43] E. Huseby, J. Gissinger, F. Candelier, N. Pujara, G. Verhille, B. Mehlig, and G. Voth, “Helical ribbons: Simple chiral sedimentation,” (2024), arXiv:2403.18157 [cond-mat.soft].
- [44] J.B. Keller and S.I. Rubinow, “Slender-body theory for slow viscous flow,” *Journal of Fluid Mechanics* **75**, 705–714 (1976).
- [45] O. Gonzalez, A.B.A. Graf, and J.H. Maddocks, “Dynamics of a rigid body in a Stokes fluid,” *Journal of Fluid Mechanics* **519**, 133–160 (2004).
- [46] T. Miara, C. Vaquero-Stainer, D. Pihler-Puzović, M. Heil, and A. Juel, “Dynamics of inertialess sedimentation of a rigid u-shaped disk,” *Communications Physics* **7**, 47 (2024).
- [47] N. Fintzi, L. Gamet, and J.-L. Pierson, “Inertial loads on a finite-length cylinder embedded in a steady uniform flow,” *Phys. Rev. Fluids* **8**, 044302 (2023).
- [48] A. S. Khair and N. G. Chisholm, “A higher-order slender-body theory for axisymmetric flow past a particle at moderate Reynolds number,” *Journal of Fluid Mechanics* **855**, 421–444 (2018).
- [49] F. Auguste, J. Magnaudet, and D. Fabre, “Falling styles of disks,” *Journal of Fluid Mechanics* **719**, 388–405 (2013).
- [50] A. Tinklenberg, M. Guala, and F. Coletti, “Thin disks falling in air,” *Journal of Fluid Mechanics* **962**, A3 (2023).
- [51] A. J. Heymsfield, “Laboratory and field observations of the growth of columnar and plate crystals from frozen droplets,” *Journal of the Atmospheric Sciences* **30**, 1650–1656 (1973).
- [52] A. Tinklenberg, M. Guala, and F. Coletti, “Turbulence effect on disk settling dynamics,” *Journal of Fluid Mechanics* **992**, A4 (2024).
- [53] E. J. Tozzi, C. T. Scott, D. Vahey, and D. J. Klingenberg, “Settling dynamics of asymmetric rigid fibers,” *Physics of Fluids* **23**, 033301 (2011).
- [54] J. Gissinger, “Dynamique d’une particule de forme quelconque en écoulement det Stokes,” (2023).

Supplemental Material: “Torques on curved atmospheric fibres”

F. Candelier,¹ K. Gustavsson,² P. Sharma,³ L. Sundberg,² A. Pumir,^{4,3} G. Bagheri,³ and B. Mehlig²

¹*Aix-Marseille Univ., CNRS, IUSTI, Marseille, France*

²*Department of Physics, Gothenburg University, Gothenburg, SE-40530 Sweden*

³*Max Planck Institute for Dynamics and Self-Organization, 37077 Göttingen, Germany*

⁴*Laboratoire de Physique, ENS de Lyon, Université de Lyon 1 and CNRS, 69007 Lyon, France*

(Dated: October 1, 2024)

In this document we summarise details regarding the theory (Sections I-V), the method of analysing the video recordings (Section VI), and the results obtained from this analysis (Section VII). This document contains 13 supplemental figures and one supplemental table.

S1. DEFINITION OF EULER ANGLES

We denote the orthogonal basis of the lab-coordinate system by $\hat{\mathbf{e}}_\alpha$, and parameterise the orientation of the body-coordinate system \mathbf{p} , \mathbf{q} , \mathbf{n} using three angles θ , ϕ , ψ as follows [see Fig. 1(a) in the main text]

$$\mathbf{n} = \begin{bmatrix} c_\phi s_\theta \\ s_\phi s_\theta \\ c_\theta \end{bmatrix}, \quad \mathbf{q} = c_\psi \begin{bmatrix} -s_\phi \\ c_\phi \\ 0 \end{bmatrix} + s_\psi \mathbf{n} \wedge \begin{bmatrix} -s_\phi \\ c_\phi \\ 0 \end{bmatrix},$$

$$\mathbf{p} = \mathbf{q} \wedge \mathbf{n}. \tag{S1}$$

where $s_\theta = \sin \theta$, $c_\phi = \cos \phi$, and so forth. Here \mathbf{p} and \mathbf{q} are orthogonal to \mathbf{n} , such that $q_z = 0$ when $\psi = 0$, and \mathbf{p} is chosen to form a right-handed coordinate system with \mathbf{q} and \mathbf{n} , see Fig. 1(a) in the main text.

This parameterisation is equivalent to Euler angles using the $Z_\phi Y_\theta Z_\psi$ convention. Assume that the particle-fixed coordinate system aligns as follows, \mathbf{p} with $\hat{\mathbf{e}}_1$, \mathbf{q} with $\hat{\mathbf{e}}_2$, and \mathbf{n} with $\hat{\mathbf{e}}_3$. First, rotate the particle-fixed coordinate system around $\hat{\mathbf{e}}_3$ by ϕ , so that the image \mathbf{p}' of $\hat{\mathbf{e}}_1$ rotates in the $\hat{\mathbf{e}}_1$ - $\hat{\mathbf{e}}_2$ -plane. The new rotated coordinate system is called \mathbf{p}' , \mathbf{q}' , $\mathbf{n}' = \mathbf{n}$. Next, rotate this coordinate system around \mathbf{q}' by θ , the polar angle. The new coordinate system is called \mathbf{p}'' , \mathbf{q}'' , \mathbf{n}'' . The third step is to rotate this coordinate system around \mathbf{n}'' by ψ . All rotations are counter-clockwise. This yields the rotation matrix for the basis vectors

$$\mathbb{R} = \begin{bmatrix} c_\phi c_\theta c_\psi - s_\phi s_\psi & -s_\phi c_\psi - c_\phi c_\theta s_\psi & c_\phi s_\theta \\ c_\phi s_\psi + s_\phi c_\theta c_\psi & c_\phi c_\psi - s_\phi c_\theta s_\psi & s_\phi s_\theta \\ -s_\theta c_\psi & s_\theta s_\psi & c_\theta \end{bmatrix}. \tag{S2}$$

The columns of \mathbb{R} are \mathbf{p} , \mathbf{q} , and \mathbf{n} . Components v_i of a vector \mathbf{v} in the lab frame map to the particle-fixed coordinate system as

$$\begin{bmatrix} v_p \\ v_q \\ v_n \end{bmatrix} = \mathbb{R}^T \begin{bmatrix} v_1 \\ v_2 \\ v_3 \end{bmatrix}. \tag{S3}$$

To make the Euler angles unique, one needs to restrict their ranges, because $[\phi, \theta, \psi]$ and $[\phi', \theta', \psi'] = [\phi + \pi, -\theta, \psi + \pi]$ (any angle modulo $\pm 2\pi$) describe the same particle orientation. For our planar fibre, the multiplicity of equivalent triplets is higher than that, because the fibre has two reflection symmetries. Applying both reflections corresponds to the matrix

$$\mathbb{S} = \begin{bmatrix} 1 & & \\ & -1 & \\ & & -1 \end{bmatrix} \tag{S4}$$

in the particle-fixed coordinate system. The rotation matrices corresponding to the two triplets $[\phi, \theta, \psi]$ and $[\phi', \theta', \psi'] = [-\phi, -\theta + \pi, \psi + \pi]$ (any angle modulo $\pm 2\pi$) are related by

$$\mathbb{S}\mathbb{R}' = \mathbb{R}. \tag{S5}$$

TABLE S1. Stokes resistance coefficients in the Stokes limit obtained using the method of Durlofsky *et al.* [1] (see text).

$2a$ [mm]	$2b$ [μm]	A_{pp} [mm]	A_{qq} [mm]	A_{nn} [mm]	B_{qn} [mm^2]	B_{nq} [mm^2]	C_{pp} [mm^3]	C_{qq} [mm^3]	C_{nn} [mm^3]
semi-circular fibres									
2	100	5.390	5.102	6.321	0.1889	-0.6331	2.027	0.5619	2.015
1	50	2.695	2.551	3.161	0.0472	-0.1583	0.2533	0.0702	0.2519
2	40	4.215	4.017	5.060	0.1194	-0.5150	1.439	0.3446	1.354
1	20	2.107	2.009	2.531	0.02985	-0.1288	0.1799	0.04307	0.1692
2	20	3.624	3.471	4.408	0.08649	-0.4485	1.186	0.2676	1.083
1	10	1.812	1.736	2.204	0.02162	-0.1121	0.1482	0.03345	0.1354
quarter-circular fibres									
2	100	6.104	4.677	6.423	0.1209	-0.6035	3.104	0.2242	3.056
1	50	3.052	2.338	3.212	0.03021	-0.1509	0.3880	0.02802	0.38204
0.5	25	1.526	1.169	1.606	0.0075	-0.0377	0.04850	0.00350	0.04776
2	40	4.831	3.579	5.125	0.07493	-0.4963	2.159	0.1207	2.094
1	20	2.416	1.790	2.562	0.01873	-0.12407	0.2699	0.01509	0.26171
2	20	4.183	3.042	4.457	0.05387	-0.4373	1.762	0.0904	1.695
1	10	2.091	1.521	2.228	0.01347	-0.1093	0.2203	0.01130	0.2118

Therefore the two triplets describe indistinguishable particle orientations. In conclusion, the four triplets $[\phi, \theta, \psi]$, $[\phi + \pi, -\theta, \psi + \pi]$, $[-\phi, -\theta + \pi, \psi + \pi]$, and $[-\phi + \pi, \theta + \pi, \psi]$ (any angle modulo $\pm 2\pi$) are equivalent because they yield indistinguishable particle orientations. We discuss in Section S7 how the angles were restricted to extract unique values of θ and ψ from the experiments.

S2. STOKES RESISTANCE COEFFICIENTS

Table S1 summarises the numerical values for the Stokes resistance coefficients for the fibres from Table 1 in the main text. The results were obtained by modeling the fibre as a chain of hydrodynamically interacting beads [1–3]. We use $N + 1$ beads of radius b to represent the fibre [Fig. 1(c) in the main text], the distance between the bead centres is thus a/N . We determine this distance by computing the resistance tensor \mathbb{A} for a slender straight wire and comparing with Eqs. (19,20) of Ref. [4], an expansion to order $(\log \kappa)^{-3}$. The smallest difference is observed for $a/N = 2.3b$. In this case the relative errors are 1.7 % for A_{\parallel} and 2.9 % for A_{\perp} for a chain with 300 beads ($\kappa \approx 344$) [5]. Here A_{\parallel} (resp. A_{\perp}) is the resistance coefficient when the fibre moves with a velocity collinear (resp. perpendicular) to its axis. Kharrouba *et al.* [6] computed the resistance coefficients to order $(\log \kappa)^{-4}$. For the chain with 300 beads, the fourth-order correction is negligible.

S3. LINEAR STABILITY ANALYSIS IN THE STOKES LIMIT

In the Stokes limit and in a quiescent fluid, Eqs. (1) and (2) in the main text admit two fixed points, $\omega^* = 0$, $v_q^* = v_n^* = 0$, $v_p^* = mg\sigma_{\psi}/(\mu A_{pp})$, $\theta^* = \pi/2$, and $\psi^* = (1 - \sigma_{\psi})\pi/2$, where $\sigma_{\psi} = \pm 1$. Close to the fixed points, we expand the dynamics as $v_p = v_p^* + \delta v_p$, and so forth. We obtain three decoupled systems of differential equations. The first system,

$$\frac{d}{dt} \delta v_p = -\frac{A_{pp\mu}}{m} \delta v_p, \quad (\text{S6a})$$

$$\frac{d}{dt} \delta \phi = -\sigma_{\psi} \delta \omega_p, \quad (\text{S6b})$$

$$\frac{d}{dt} \delta \omega_p = -\frac{C_{pp\mu}}{J_{pp}} \delta \omega_p, \quad (\text{S6c})$$

describes how δv_p and $\delta \omega_p$ decay exponentially towards zero. Here J_{pp} (and J_{qq}, J_{nn}) are the non-zero elements of the particle-inertia tensor \mathbb{J} in the particle-fixed basis. The angle ϕ goes to an undetermined constant ϕ^* (a consequence

of rotational symmetry around \mathbf{g}). The second system,

$$\frac{d}{dt}\delta v_q = -\frac{A_{qq}\mu}{m}\delta v_q - \left[\frac{B_{nq}\mu}{m} + \frac{mg\sigma_\psi}{A_{pp}\mu}\right]\delta\omega_n - g\sigma_\psi\delta\psi, \quad (\text{S7a})$$

$$\frac{d}{dt}\delta\psi = \delta\omega_n, \quad (\text{S7b})$$

$$\frac{d}{dt}\delta\omega_n = -\frac{\mu}{J_{nn}}[C_{nn}\delta\omega_n + B_{nq}\delta v_q], \quad (\text{S7c})$$

has three stability exponents $\lambda_1, \dots, \lambda_3$, obtained by solving a third-order equation. In the underdamped limit of large rotational inertia J_{nn} we obtain

$$\lambda_{1,2} \sim \frac{1}{2A_{qq}J_{nn}} \left[\sigma_\psi \frac{B_{nq}gm^2}{\mu} \left(\frac{1}{A_{pp}} - \frac{1}{A_{qq}} \right) - \mu(A_{qq}C_{nn} - B_{nq}^2) \right] \pm i\sqrt{-\sigma_\psi \frac{B_{nq}mg}{A_{qq}J_{nn}}}, \quad (\text{S8a})$$

$$\lambda_3 \sim -\frac{A_{qq}\mu}{m}. \quad (\text{S8b})$$

Since $A_{qq}C_{nn} - B_{nq}^2 > 0$, the dynamics damps to zero in the absence of gravity. With gravity, the fixed point with $\sigma_\psi = 1$, $\psi^* = 0$, is stable. This follows because our particles have $A_{pp} > A_{qq}$ and $B_{nq} < 0$. In this underdamped limit, the variables v_q , ψ , and ω_q exhibit transient oscillations. Their angular velocity can be read off from the imaginary part of $\lambda_{1,2}$. Consider instead the overdamped limit (m and J_{nn} small). In this limit, one observes the same steady state, but the transient does not exhibit oscillations. The third system,

$$\frac{d}{dt}\delta v_n = -\frac{A_{nn}\mu}{m}\delta v_n - \left[\frac{B_{qn}\mu}{m} - \frac{mg\sigma_\psi}{A_{pp}\mu}\right]\delta\omega_q + g\delta\theta, \quad (\text{S9a})$$

$$\frac{d}{dt}\delta\theta = \sigma_\psi\delta\omega_q, \quad (\text{S9b})$$

$$\frac{d}{dt}\delta\omega_q = -\frac{\mu}{J_{qq}}[C_{qq}\delta\omega_q + B_{qn}\delta v_n], \quad (\text{S9c})$$

is similar to Eq. (S8). However, frequencies and bifurcations may differ depending on the numerical values of the resistance coefficients and upon the moments of inertia. This means that there may be parameter regimes where θ decays without oscillations while ψ oscillates, or vice versa.

Evaluating the stability exponents of Eqs. (S7) and (S9) for the semi-circular fibres in Table S1 shows that the fixed point $\psi^* = 0$ ($\sigma_\psi = 1$) is stable in the Stokes limit. Both sub-systems predict oscillations for all semi-circular fibres from Table 1 in the main text, except for the fibres with $\kappa = 100$ and $L = 1\text{mm}$, which do not show oscillations at all.

Moreover, the period time for the dynamics (S9) is larger than that of the dynamics (S7) by approximately a factor 2 for all cases showing oscillations. The time scale of damping is significantly smaller than the period time, with the exception of the $\kappa = 50$ and $L = 2\text{mm}$ semi-circular fibre. In conclusion, oscillations in the experiments are expected to be slightly easier to be seen in $\psi(t)$, but only if the initial $\psi(t=0)$ is significantly different from zero (or if the initial $\omega_n(t=0)$ is different from zero).

We note that if B_{nq} and B_{qn} have the same sign, both fixed points $\psi^* = 0$ and $\psi^* = \pi$ are unstable. This is the case for taco-shaped disks which continue to rotate as they settle [7], they do not align. This follows from the analysis described above, by solving $\mathbf{F}_h^{(0)} + \mathbf{F}_g = 0$ and $\mathbf{T}_h^{(0)} = 0$ for \mathbf{v}^* and $\boldsymbol{\omega}^*$, just as in Ref. [3]. In this way one obtains ψ as a function θ :

$$\sin\psi \sin\theta = C_0 \cos(\theta) - \frac{B_{nq}(A_{nn}C_{qq} - B_{qn}^2)}{B_{qn}(A_{qq}C_{nn} - B_{nq}^2)} \quad (\text{S10})$$

with constant of motion C_0 (the full solution is found from (S10) by reflections). The resulting phase portrait forms bands of closed orbits around center fixed-points separated by manifolds connecting saddle points at $\psi^* = m\pi$ and $\theta^* = n\pi$ with integer values of m and n . This explains Fig. 5 in Ref. [7] which shows one half the phase portrait. Such phase portraits were also obtained by numerical simulation in Ref. [7]. Gonzalez *et al.* [8] discuss the settling angular dynamics of asymmetric particles in the Stokes limit solely in terms of mobility matrix $\mathbb{b} = (\mathbb{B}^T - \mathbb{A}\mathbb{B}^{-1}\mathbb{C})^{-1}$. This is consistent with Eq. (S10), because it can be expressed entirely in terms of elements of \mathbb{b} : the exponent in Eq. (S10) is just $-b_{qn}/b_{nq}$. Our linear stability analysis shows, however, that the mobility matrix \mathbb{b} alone does not suffice to determine the approach of the steady state.

S4. SLENDER-BODY THEORY TO ORDER Re_a

Khayat and Cox [9] computed the hydrodynamic force per unit length $\mathbf{f}_h(s)$ on a segment of a slender body held

fixed in a uniform flow $\mathbf{u} = u\hat{\mathbf{u}}$,

$$\mathbf{f}_h = 2\pi\rho_f\nu ua^2 \left\{ (\mathbf{t}\mathbf{t}^\top - 2\mathbb{1})\hat{\mathbf{u}} \frac{1}{\log \kappa} + \left[(\mathbf{t}\mathbf{t}^\top - 2\mathbb{1})(\mathbf{J} + \hat{\mathbf{u}} \log 2\epsilon) + \left(\frac{3}{2}\mathbf{t}\mathbf{t}^\top - \mathbb{1}\right)\hat{\mathbf{u}} \right] \frac{1}{(\log \kappa)^2} + \dots \right\}, \quad (\text{S11a})$$

$$\mathbf{J}(s) = \frac{1}{4} \left(\int_{-1}^{s-\epsilon} + \int_{s+\epsilon}^1 \right) ds' \mathbb{G}(\mathbf{x} - \mathbf{x}') (2\mathbb{1} - \mathbf{t}'\mathbf{t}'^\top) \hat{\mathbf{u}}, \quad (\text{S11b})$$

$$G_{ij}(\mathbf{x}) = \delta_{ij} \Delta \Psi - \partial_i \partial_j \Psi(\mathbf{x}), \quad \text{with} \quad \Psi(\mathbf{x}) = \frac{2}{\text{Re}_a} \int_0^{\xi_1} d\xi \frac{1 - e^{-\xi}}{\xi} \quad \text{and} \quad \xi_1 = \frac{1}{2} \text{Re}_a (x - \hat{\mathbf{u}} \cdot \mathbf{x}). \quad (\text{S11c})$$

Here $\mathbf{x} = \mathbf{x}(s)$ and $\mathbf{x}' = \mathbf{x}(s')$ are locations along the contour of the fibre, made non-dimensional by dividing by a , and parameterised by s and s' . The corresponding tangent vectors are $\mathbf{t} = \mathbf{t}(s)$ and $\mathbf{t}' = \mathbf{t}(s')$. The infinitesimal positive ϵ is introduced because the integrand has a singularity at $s = s'$ (a divergence for Stokes contribution, a finite jump for Re_a -contribution). Khayat and Cox [9] used Eq. (S11) to compute force and torque on a straight fibre.

From $\mathbf{f}_h(s)$, force and torque w.r.t. to the centre-of-mass \mathbf{x}_{com} are computed by line integrals

$$\mathbf{F}_h = a \int_{-1}^1 ds \mathbf{f}_h(s), \quad (\text{S12a})$$

$$\mathbf{T}_h = a \int_{-1}^1 ds [\mathbf{x}(s) - \mathbf{x}_{\text{com}}] \wedge \mathbf{f}_h(s) \quad (\text{S12b})$$

along the fibre. To perform the integrals, we parameterise the curved planar fibres as

$$\mathbf{x}(s) = \mathbf{x}_0 + R\mathbf{p} \cos\left(\frac{\pi}{M}s\right) + R\mathbf{q} \sin\left(\frac{\pi}{M}s\right), \quad (\text{S13})$$

where $R = M/\pi$ is the non-dimensional radius of curvature, $M = 2$ for a semi-circle and $M = 4$ for a quarter circle. The centre-of-mass \mathbf{x}_{com} is determined by

$$\mathbf{x}_{\text{com}} - \mathbf{x}_0 = \mathbf{p} \frac{R}{2} \int_{-1}^1 ds \cos\left(\frac{\pi}{M}s\right) = \mathbf{p} \left(\frac{M}{\pi}\right)^2 \sin\left(\frac{\pi}{M}\right). \quad (\text{S14})$$

To compute the fluid-inertia contribution to force and torque at small but non-zero Re_a , we extract from Eqs. (S11) the contributions linear in Re_a , by a Re_a -expansion of $\Psi(\mathbf{x})$. It follows that to order Re_a , the fluid-inertia contribution to force and torque is given by

$$\mathbf{f}_h^{(1)} = 2\pi\rho_f\nu u (\mathbf{t}\mathbf{t}^\top - 2\mathbb{1}) \mathbf{J}^{(1)} / (\log \kappa)^2, \quad (\text{S15a})$$

$$\mathbf{J}^{(1)}(s) = \frac{1}{4} \int_{-1}^1 ds' \mathbb{G}^{(1)}(\mathbf{x} - \mathbf{x}') (2\mathbb{1} - \mathbf{t}'\mathbf{t}'^\top) \hat{\mathbf{u}}, \quad (\text{S15b})$$

$$G_{ij}^{(1)}(\mathbf{x}) = \delta_{ij} \Delta \Psi^{(1)} - \partial_i \partial_j \Psi^{(1)}(\mathbf{x}), \quad \text{with} \quad \Psi^{(1)}(\mathbf{x}) = -\frac{1}{8} \text{Re}_a (\sqrt{|\mathbf{x}|^2} - \hat{\mathbf{u}} \cdot \mathbf{x})^2. \quad (\text{S15c})$$

To order Re_a , Eq. (S15) shows that the fluid inertia torque contains at most three powers of \hat{u}_p , \hat{u}_q , and \hat{u}_n . Evaluating the integrals (S15b) and (S12b), we obtain

$$T_{p,M}^{(1)} / (2\pi\mu ua^2) = \frac{au}{\nu(\log \kappa)^2} a_{p,M} \hat{u}_q \hat{u}_n, \quad (\text{S16a})$$

$$T_{q,M}^{(1)} / (2\pi\mu ua^2) = \frac{au}{\nu(\log \kappa)^2} a_{q,M} \hat{u}_p \hat{u}_n, \quad (\text{S16b})$$

$$T_{n,M}^{(1)} / (2\pi\mu ua^2) = \frac{au}{\nu(\log \kappa)^2} [a_{n,M} \hat{u}_q \hat{u}_p - b_{n,M} \hat{u}_q - c_{n,M} \hat{u}_q \hat{u}_n^2 - d_{n,M} \hat{u}_q^3]. \quad (\text{S16c})$$

This is Eq. (4) in the main text, with $\mathbf{v} = -\mathbf{u}$. As explained there, M parameterises the central angle $2\pi/M$ of the circle segment. For the coefficients we find:

$$a_{p,M} = -\frac{M^2}{36\pi^3} [84\pi - M(57s_{1,M} + 12s_{2,M} + s_{3,M})], \quad (\text{S17a})$$

$$a_{q,M} = \frac{M^2}{36\pi^4} [84\pi^2 + 3M^2(-2 + c_{1,M} + 2c_{2,M} - c_{3,M}) - M\pi(105s_{1,M} - 12s_{2,M} + s_{3,M})], \quad (\text{S17b})$$

$$a_{n,M} = \frac{M^3}{48\pi^4} s_{1,M} [12\pi(1 - c_{2,M}) + M(16s_{1,M} - 6s_{2,M} - s_{4,M})], \quad (\text{S17c})$$

$$b_{n,M} = \frac{M^2}{32\pi^4} s_{1,M} [12\pi^2 + M^2(1 - c_{4,M}) - 10M\pi s_{2,M}], \quad (\text{S17d})$$

$$c_{n,M} = -\frac{M^2}{64\pi^4} s_{1,M} (2\pi - Ms_{2,M})^2, \quad (\text{S17e})$$

$$d_{n,M} = \frac{M^3}{32\pi^4} s_{1,M} s_{2,M} (2\pi - Ms_{2,M}), \quad (\text{S17f})$$

where $c_{n,M} = \cos(n\pi/M)$ and $s_{n,M} = \sin(n\pi/M)$. Evaluating $\mathbf{T}^{(1)}$ for large values of M using Eqs. (S16) and (S17), we find that $T_q^{(1)} \rightarrow 0$ while $T_p^{(1)}$ and $T_n^{(1)}$ combine to the torque on a slender straight wire, $\mathbf{T}^{(1)} = -\frac{5\pi}{3}\rho_f a^3(\mathbf{q} \cdot \mathbf{v})(\mathbf{q} \wedge \mathbf{v})/(\log \kappa)^2$, where \mathbf{q} is the vector along the symmetry axis of the straight wire. This result is consistent with Eqs. (6.19) and (6.22) of Khayat and Cox [9] for a straight fibre. For a ring ($M = 1$) we find $\mathbf{T}^{(1)} = 14a^3(\mathbf{n} \cdot \mathbf{v})(\mathbf{n} \times \mathbf{v})\rho_f/(3\pi(\log \kappa)^2)$. Here \mathbf{n} is the unit vector along the particle symmetry axis. The fluid-inertia torques for ring and rod have opposite signs, as expected [10, 11].

S5. SLENDER-BODY THEORY TO HIGHER ORDERS OF Re_a

To compare with experiments, we must deal with the fact that Re_a is not small, so that (S16) and the corresponding corrections for the force do not directly apply. The standard procedure is to account for higher Re_a by parameterisations of the fluid-inertia corrections. For particles with axisymmetry and fore-aft symmetry this is straightforward for Re_a up to the order of ten [11–13].

For our slender curved fibres, we can use the full slender-body theory from Ref. [9] to evaluate fluid-inertia contributions to torque and force for larger Re_a . To this end, we subtract the Stokes contribution ($\text{Re}_a = 0$) from Eqs. (S11) to obtain a set of equations on the same form as Eqs. (S15), but with $\Psi^{(1)}(\mathbf{x})$ replaced by the fluid-inertia contribution

$$\Psi^{(i)}(\mathbf{x}) = \frac{2}{\text{Re}_a} \int_0^{\xi_1} d\xi \left(\frac{1 - e^{-\xi}}{\xi} - 1 \right) \quad \text{with} \quad \xi_1 = \frac{1}{2}\text{Re}_a(x - \hat{\mathbf{u}} \cdot \mathbf{x}). \quad (\text{S18})$$

The resulting set of equations yields the fluid inertia forces and torques for our fibres for any Re_a within the slender-body approximation of Khayat and Cox [9]. Since we could not evaluate the resulting integrals [Eqs. (S11b) and (S12)] in closed form, we resorted to numerical integration. In this we obtained the fluid-inertia corrections to force and torque in the particle-fixed basis as functions of Re_a and the orientation of $\hat{\mathbf{u}}$. We checked that the numerical results simplify to Eq. (4) in the main text in the limit of small Re_a .

Our numerical results show that the analysis performed in the limit of small Reynolds numbers in the main text is qualitatively unchanged, but there are quantitative differences: the steady state remains at $\omega^* = 0$, $\psi^* = 0$, and $v_q^* = 0$, but the values of θ^* , v_p^* , and v_n^* obtain corrections due to the force contribution from fluid inertia, and because Re_a is not infinitesimal. Moreover, the location of the pitchfork bifurcation changes, it is no longer given by Eq. (6) in the main text. We determine θ^* , v_p^* , and v_n^* by evaluating the fluid-inertia corrections $F_p^{(i)}(\text{Re}_a, \beta)$, $F_n^{(i)}(\text{Re}_a, \beta)$ and $T_q^{(i)}(\text{Re}_a, \beta)$ with $\omega^* = \psi^* = v_q^* = 0$ (the other force and torque components are zero at this point) numerically for a large number of values of Re_a and β . Here β is the angle between \mathbf{n} and the velocity \mathbf{v} (see Fig. S1), and $\text{Re}_a = av^*/\nu$ is the particle Reynolds number defined in the main text.

The steady states are obtained by finding the values Re_a^* , β^* and θ^* that solve the system

$$F_p = -\mu A_{pp}v_p + F_p^{(i)}(\text{Re}_a, \beta) + mg \sin \theta = 0, \quad (\text{S19a})$$

$$F_n = -\mu A_{nn}v_n + F_n^{(i)}(\text{Re}_a, \beta) - mg \cos \theta = 0, \quad (\text{S19b})$$

$$T_q = -\mu B_{qn}v_n + T_q^{(i)}(\text{Re}_a, \beta) = 0, \quad (\text{S19c})$$

where $v_n = v \cos \beta$, $v_p = v\sqrt{1 - \cos^2 \beta}$ and $v = \text{Re}_a\nu/a$. Eq. (S19) has one fixed point with $\theta^* = \pi/2$ and $v_n^* = 0$ as in the Stokes limit, but v_p^* , obtained by solving $-\mu A_{pp}v_p + F_p^{(i)}(\text{Re}_a, \pi/2) + mg = 0$, takes lower values due to the inertial correction $F_p^{(i)}$.

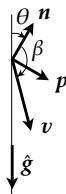


FIG. S1. *Parameterisation of inertial torque at larger Re_a .* Definition of the angle β used to parameterise fluid-inertia corrections to force and torque for larger Re_a . The vectors \mathbf{p} and \mathbf{n} are part of the particle-fixed coordinate system [Fig. 1(a) in the main text], θ is the tilt angle, \mathbf{v} is the settling velocity, and $\hat{\mathbf{g}}$ is the direction of gravity. The four vectors \mathbf{p} , \mathbf{n} , \mathbf{v} , and $\hat{\mathbf{g}}$ lie in the same plane.

This fixed point becomes unstable in a pitchfork bifurcation, as described in the main text. The location of the bifurcation is determined by first solving $\lim_{v_n \rightarrow 0} T_q/v_n$ for v_p , and then inserting the resulting solution together with $\theta = \beta = \pi/2$ into the expression for F_p . The bifurcation occurs at parameter values where $F_p = 0$. The sign of F_p for a given set of parameters tells whether the system is before ($F_p < 0$) or after ($F_p > 0$) the bifurcation. After the bifurcation, we numerically solve Eqs. (S19) to obtain the stable fixed points θ^* and $v_g^* = -v_n^* \cos \theta^* + v_p^* \sin \theta^*$ shown in Fig. 3 in the main text.

S6. DATA ANALYSIS

Tatsii *et al.* [14] measured the settling speeds of straight and curved slender fibres in quiescent air using the Göttingen turret [13]. Here we extracted fibre orientation from the video recordings of Tatsii *et al.* [14], to determine how shape-symmetry breaking affects the angular dynamics of the settling fibres. The Göttingen turret has two pairs of cameras, top and bottom. The two cameras in a pair are orthogonal to each other in a plane perpendicular to the direction of gravity. Details of the setup are described by Bhowmick *et al.* [13]. The fibers used in our experiments were precisely created using a 3D printer, specifically the Photonic Professional GT model by Nanoscribe GmbH (2015), capable of achieving a printing precision of $< 1\mu\text{m}$. The fibres were printed by polymerising acrylic resin IP-S ($\text{CH}_{1.27}\text{N}_{0.086}\text{O}_{0.37}$) with density of 1200 kg/m^3 . The uniform polymerisation of the resin during printing and subsequent curing, combined with the fact that the printer always produces a solid body without voids, minimises variations in particle density. The 3D printer requires the 3D CAD models of the fibres to produce the fibers. To check for possible defects that could lead to deviations in fibre size and shape, we examined all fibres under a microscope after printing and the defected ones are removed from the batch as explained in [14]. All remaining ones were found to match the expected geometric specifications. See Figure S1 in the supplementary material by Tatsii *et al.* [14] for example photos and 3D scan profiles of particles taken after printing.

We analysed all experiments where the fibre was visible and in focus in at least in one camera pair (top and/or bottom), in order to obtain reliable estimates for the fibre orientation. In their analysis of the setting speed, Tatsii *et al.* [14] also considered experiments where the fibre is not captured by all cameras. Therefore the number N of experiments analysed here is smaller than in Table 1 in Ref. [14].

Fibre orientations were tracked in a three-stage process: firstly, experimental images are pre-processed; secondly, synthetic projection images of fibres with different orientations were created using their 3D CAD models; and finally, fibre orientations were extracted by matching experimental and synthetic projection images. During pre-processing, all frames corresponding to a given fibre were cropped to a uniform size. This guarantees that the entire projection of the fibre is contained in the frame, regardless of fibre orientation. Each fibre image was then shifted so that the left edge of the frame such the top left corner of the rectangular box bounding the particle image was in the same pixel for all images. A fixed threshold based on the entire camera field of view was used for binarization of the particle images. However, it was found that shifting all thresholded images to the left triggered greater sensitivity in finding the best match for quarter circles and some of the larger semi-circles (specifically hc 2000x40 E06 and hc 2000x20 E08). This was attributed to the bounding box being wider than the rest for most of these fibres and/or various possible experimental uncertainties (as outlined below). As a result, we re-analysed data obtained for these cases by determining a threshold for each cropped image and adjusting the matching library database to contain a finer angular resolution (see below).

To create synthetic images, we used the 3D-CAD model employed for printing the fibres. we varied the Euler angles of the fibre 3D model, with resolution $\delta\phi = 0.02\pi$, $\delta\theta = 0.01\pi$, $\delta\psi = 0.02\pi$ for most semi-circles and $\delta\phi = 0.02\pi$, $\delta\theta = 0.005\pi$, $\delta\psi = 0.005\pi$ for quarter circles and some semi-circles. We projected the 3D model to the two orthogonal camera planes such that the size of the largest dimension of the produced image (in pixels) was L/r , where L is the length of the largest dimension of the fibre in μm and r is the effective camera resolution in μm per pixel, i.e. $6.75\ \mu\text{m}/\text{pixel}$. This ensures that the size of synthetic images matches those captured by the cameras. The best match between experimental and synthetic image was selected to be the one with the smallest pixel-wise distance summed over views of the camera pair.

The shape symmetry of the fibres implies that there are four equivalent triplets of Euler angles for a given fibre orientation (Section S1). To resolve this ambiguity in Figs. S2 and S3, we chose time series of Euler angles that yield continuous smooth trajectories. For the other experimental data shown in Appendix S7, we constrained the angles as follows: θ to the interval $[0, \pi/2]$, and ψ to $[-\pi/2, \pi/2]$.

Our analysis is subject to the following errors. In some cases, out-of-focus images give rise to distorted projections, so that maximising pixel-wise overlap may cause systematic errors. The size of the experimental fibre projection may deviate from the expected dimension for a number of reasons. These include changes in magnification along the camera axis, slight blurring of the particle image, and imprecise thresholding. Quantifying these errors is challenging, as they are likely to vary independently across different experiments. However, based on the standard deviation values

reported in Table 1 in the main text, their impact on the measured angles appears to be small. Camera misalignment can be ruled out as a source of error as three-dimensional camera calibrations revealed that the angles between the two cameras in a pair deviate by less than 1 degree from a perfect right angle. The temperature in the room is maintained at about 22.4 °C during the experiments. To estimate the maximum possible change in air temperature in the settling chamber, we observed an increase of about 1 degree when the LED runs continuously for 15 minutes (normally it runs for a few seconds every few minutes). This conservative estimate of the temperature increase can change the viscosity of the air by a maximum of 1%.

It should be noted that the initial conditions of the particles injected into the settling chamber, including the initial release velocity, angular velocity and orientation, are not the same between the different experimental runs. Variations in transient dynamics can occur since the images are taken at a fixed distance from the injection site, even if the particles have the same shape, see Fig. S3. The differences observed in cases that appear to have reached a steady state, are likely due to other experimental uncertainties. However, the low scatter of the experimental results, as indicated by the low value of the standard deviation, suggests that they are highly reliable.

S7. SUMMARY OF EXPERIMENTAL RESULTS

Figures S2 and S3 show the angles extracted from video recordings of Ref. [14] as described in Appendix S6. Shown are results for two different semi-circular fibres. Figures S4 to S13 show snapshots of the projections of steadily settling fibres in onto the camera planes of the bottom cameras.

-
- [1] L. Durlofsky, J. F. Brady, and G. Bossis, “Dynamic simulation of hydrodynamically interacting particles,” *Journal of Fluid Mechanics* **180**, 21–9 (1987).
 - [2] D. Collins, R.J. Hamati, F. Candelier, K. Gustavsson, B. Mehlig, and G.A. Voth, “Lord Kelvin’s isotropic helicoid,” *Physical Review Fluids* **6**, 074302 (2021).
 - [3] E. Huseby, J. Gissinger, F. Candelier, N. Pujara, G. Verhille, B. Mehlig, and G. Voth, “Helical ribbons: Simple chiral sedimentation,” (2024), arXiv:2403.18157 [cond-mat.soft].
 - [4] J.B. Keller and S.I. Rubinow, “Slender-body theory for slow viscous flow,” *Journal of Fluid Mechanics* **75**, 705–714 (1976).
 - [5] J. Gissinger, “Dynamique d’une particule de forme quelconque en écoulement de Stokes,” (2023).
 - [6] Mohammed Kharrouba, Jean-Lou Pierson, and Jacques Magnaudet, “Flow structure and loads over inclined cylindrical rodlike particles and fibers,” *Phys. Rev. Fluids* **6**, 044308 (2021).
 - [7] T. Miara, C. Vaquero-Stainer, D. Pihler-Puzović, M. Heil, and A. Juel, “Dynamics of inertialess sedimentation of a rigid u-shaped disk,” *Communications Physics* **7**, 47 (2024).
 - [8] O. Gonzalez, A.B.A. Graf, and J.H. Maddocks, “Dynamics of a rigid body in a Stokes fluid,” *Journal of Fluid Mechanics* **519**, 133–160 (2004).
 - [9] R.E. Khayat and R.G. Cox, “Inertia effects on the motion of long slender bodies,” *Journal of Fluid Mechanics* **209**, 435–462 (1989).
 - [10] V. Dabade, N. K. Marath, and G. Subramanian, “Effects of inertia and viscoelasticity on sedimenting anisotropic particles,” *J. Fluid Mech.* **778**, 133–188 (2015).
 - [11] F. Jiang, L. Zhao, H. I. Andersson, K. Gustavsson, A. Pumir, and B. Mehlig, “Inertial torque on a small spheroid in a stationary uniform flow,” *Phys. Rev. Fluids* **6**, 024302 (2021).
 - [12] A. Roy, S. Kramel, U. Menon, G.A. Voth, and D.L. Koch, “Orientation of finite Reynolds number anisotropic particles settling in turbulence,” *Journal of Non-Newtonian Fluid Mechanics* **318**, 105048 (2023).
 - [13] T. Bhowmick, J. Seesing, K. Gustavsson, J. Guettler, Y. Wang, A. Pumir, B. Mehlig, and G. Bagheri, “Inertia induces strong orientation fluctuations of nonspherical atmospheric particles,” *Phys. Rev. Lett.* **132**, 034101 (2024).
 - [14] D. Tatsii, S. Bucci, T. Bhowmick, J. Guettler, L. Bakels, G. Bagheri, and A. Stohl, “Shape matters: Long-range transport of microplastic fibers in the atmosphere,” *Environmental Science & Technology* **58**, 671–682 (2024).

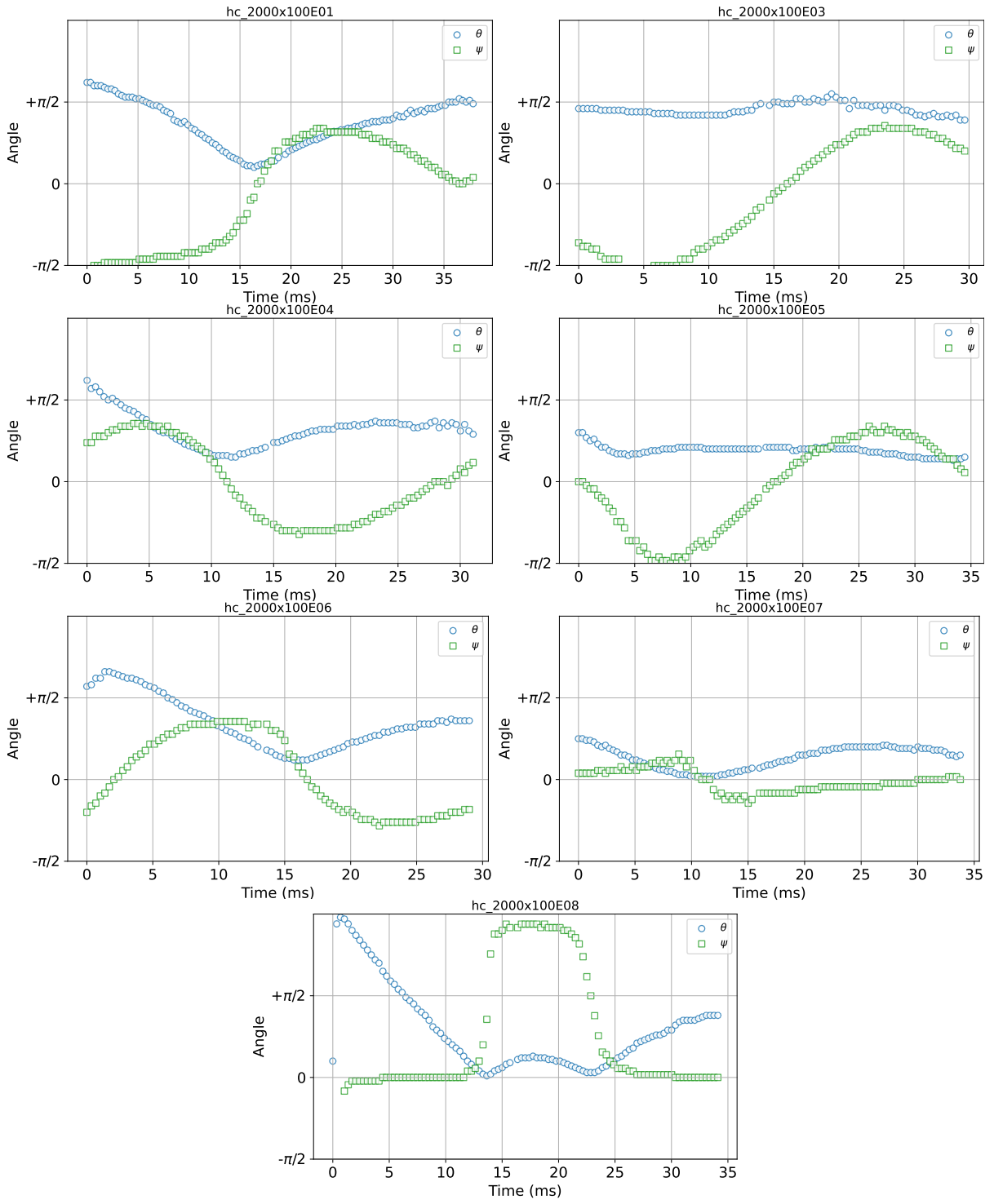


FIG. S2. Semi-circular fibres with aspect ratio $\kappa = 20$, length $L = 2000 \mu\text{m}$, and diameter $d = 100 \mu\text{m}$. Shown are the angles θ and ψ from upper and lower cameras.

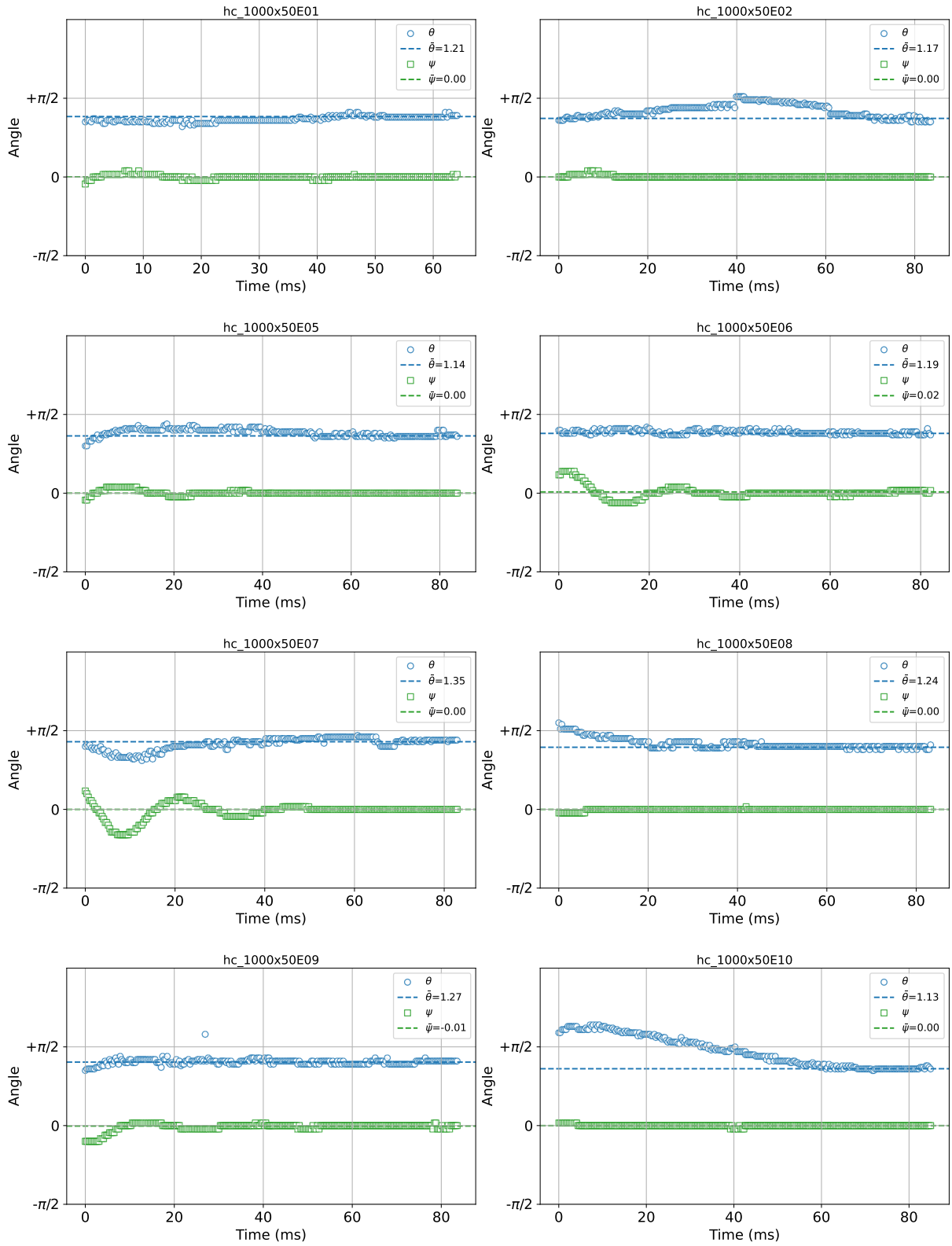


FIG. S3. Semi-circular fibres with with aspect ratio $\kappa = 20$, length $L = 1000 \mu\text{m}$, and diameter $d = 50 \mu\text{m}$. Shown are the angles θ and ψ from upper and lower cameras, as well as the average angles (averaged over the frames from the bottom cameras).



FIG. S4. Snapshots of steady state for semi-circular fibres with with aspect ratio $\kappa = 20$, length $L = 1000 \mu\text{m}$, and diameter $d = 50 \mu\text{m}$. Shown are the fibres observed in the planes of the bottom cameras towards the end of experimental run (red), as well as the extracted orientation (blue).

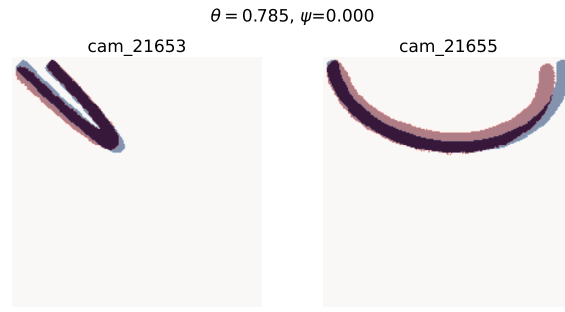


FIG. S5. Same, for semi-circular fibre with aspect ratio $\kappa = 50$, length $L = 2000 \mu\text{m}$, and diameter $d = 40 \mu\text{m}$.

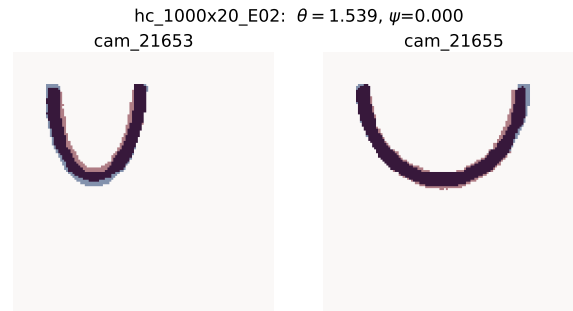


FIG. S6. Same, for semi-circular fibre with aspect ratio $\kappa = 50$, length $L = 1000 \mu\text{m}$, and diameter $d = 20 \mu\text{m}$.

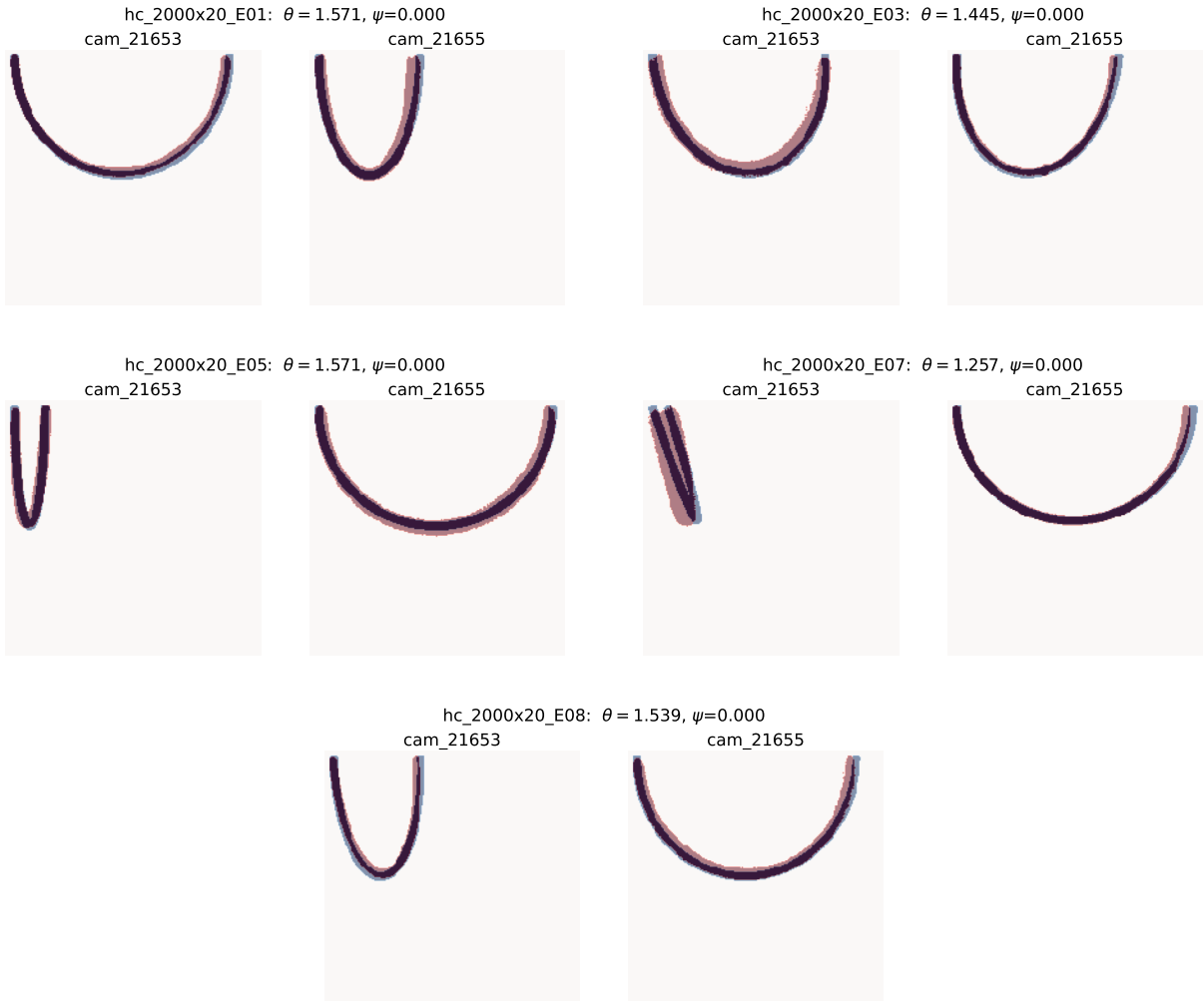


FIG. S7. Same, for semi-circular fibres with aspect ratio $\kappa = 100$, length $L = 2000 \mu\text{m}$, and diameter $d = 20 \mu\text{m}$.



FIG. S8. Same, for quarter-circular fibres with aspect ratio $\kappa = 20$, length $L = 1000 \mu\text{m}$, and diameter $d = 50 \mu\text{m}$.

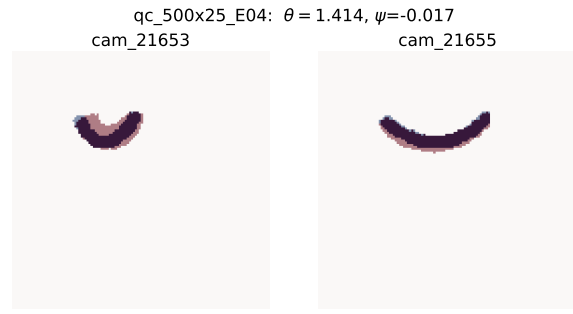


FIG. S9. Same, for quarter-circular fibre with aspect ratio $\kappa = 20$, length $L = 500 \mu\text{m}$, and diameter $d = 25 \mu\text{m}$.

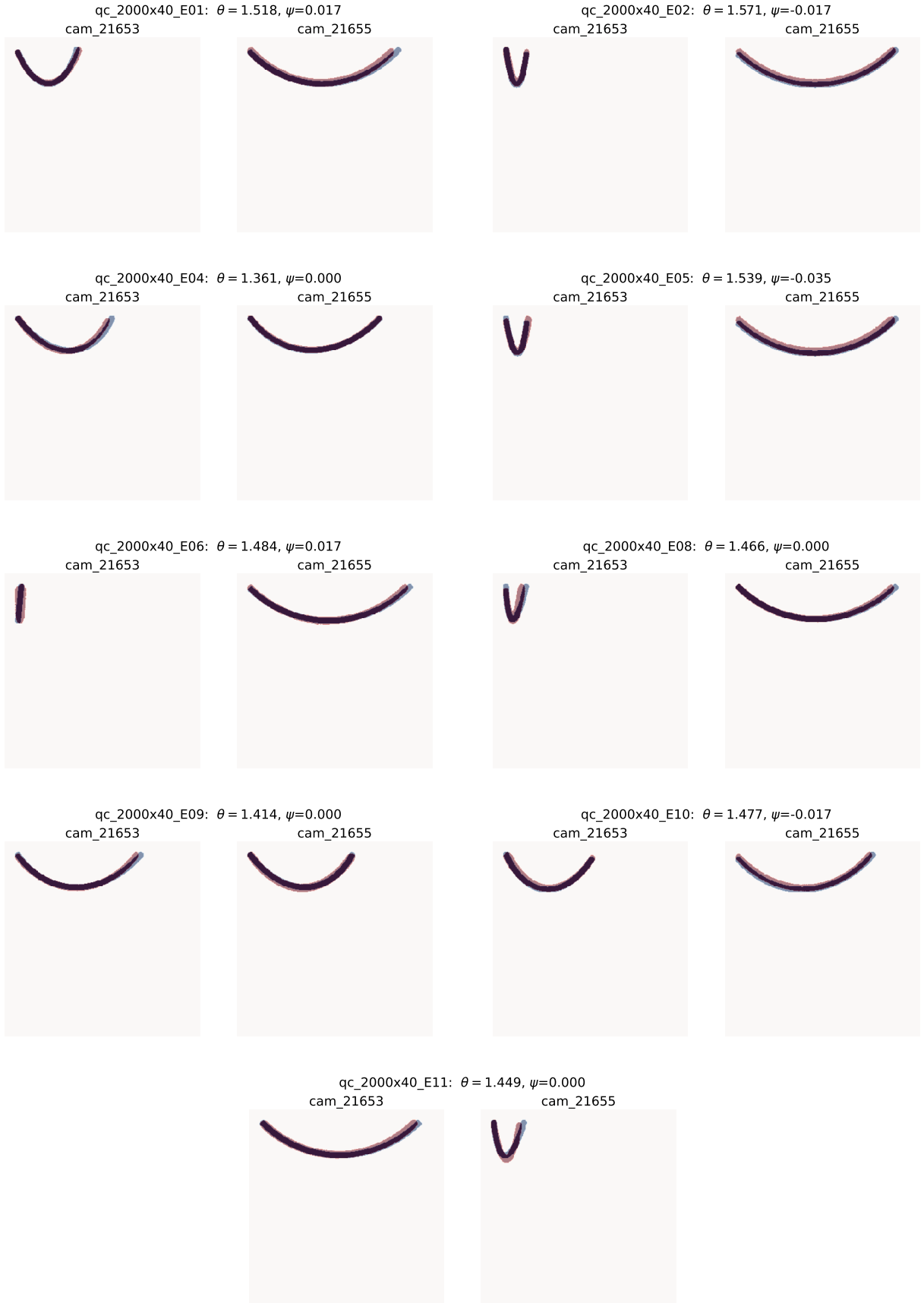
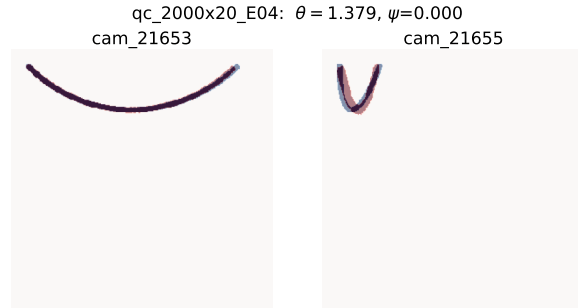


FIG. S10. Same, for quarter-circular fibres with aspect ratio $\kappa = 50$, length $L = 2000 \mu\text{m}$, and diameter $d = 40 \mu\text{m}$.



FIG. S11. Fig. S10 continued.

FIG. S12. Same, for quarter-circular fibre with aspect ratio $\kappa = 50$, length $L = 1000 \mu\text{m}$, and diameter $d = 20 \mu\text{m}$.FIG. S13. Same, for quarter-circular fibre with aspect ratio $\kappa = 100$, length $L = 2000 \mu\text{m}$, and diameter $d = 20 \mu\text{m}$.